Appl. Math. Mech. -Engl. Ed., **42**(10), 1423–1438 (2021)

APPLIED MATHEMATICS AND MECHANICS (ENGLISH EDITION)

https://doi.org/10.1007/s10483-021-2780-6

Clamped-end effect on static detection signals of DNA-microcantilever*

Junzheng WU, Nenghui ZHANG†

Shanghai Institute of Applied Mathematics and Mechanics, Shanghai Key Laboratory of Mechanics in Energy Engineering, School of Mechanics and Engineering Science, Shanghai University, Shanghai 200072, China

(Received May 30, 2021 / Revised Aug. 13, 2021)

Abstract Boundary constraint induced inhomogeneous effects are important for mechanical responses of nano/micro-devices. For microcantilever sensors, the clamped-end constraint induced inhomogeneous effect of static deformation, so called the clamped-end effect, has great influence on the detection signals. This paper is devoted to developing an alternative mechanical model to characterize the clamped-end effect on the static detection signals of the DNA-microcantilever. Different from the previous concentrated load models, the DNA adsorption is taken as an equivalent uniformly distributed tangential load on the substrate upper surface, which exactly satisfies the zero force boundary condition at the free-end. Thereout, a variable coefficient differential governing equation describing the non-uniform deformation of the DNA-microcantilever induced by the clamped-end constraint is established by using the principle of minimum potential energy. By reducing the order of the governing equation, the analytical solutions of the curvature distribution and static bending deflection are obtained. By comparing with the previous approximate surface stress models, the clamped-end effect on the static deflection signals is discussed, and the importance of the neutral axis shift effect is also illustrated for the asymmetric laminated microcantilever.

Key words surface stress, DNA adsorption, microcantilever biosensor, static deflection, clamped-end effect, non-uniform deformation

Chinese Library Classification O472$^+$.1
2010 Mathematics Subject Classification 74B10

1 Introduction

During the past decades, nano/micro-beam based detection sensors have received significant attention due to their benefits of extreme sensitivity, fast response, low cost, and high integratability[1]. Driven by those remarkable physical properties, nano/micro-beam sensors

* Citation: WU, J. Z. and ZHANG, N. H. Clamped-end effect on static detection signals of DNA-microcantilever. *Applied Mathematics and Mechanics* (*English Edition*), **42**(10), 1423–1438 (2021) https://doi.org/10.1007/s10483-021-2780-6

† Corresponding author, E-mail: nhzhang@shu.edu.cn

Project supported by the National Natural Science Foundation of China (Nos. 11772182, 11272193, and 10872121) and the Program of Shanghai Municipal Education Commission (No. 2019-01-07-00-09-E00018)

have been widely used in the detection of metal atoms, gas molecules, and biomolecules based on the atomic force microscope or time-resolved spectroscopy technology[2–4]. Numerous studies have revealed that the prominent surface effect on the mechanical behaviors of nano/micro-devices increases with the decrease in the microstructure characteristic scale[5–6]. Various numerical approaches have also been developed to characterize the influence of surface effects on the mechanical properties of nano/micro-materials, such as classical molecular dynamics (MD)[7–8] and finite element method (FEM)[9–12]. Nevertheless, the remain misunderstanding of the underlying physical mechanism in surface effect seriously impedes the further development of microcantilever-based detection technology.

From the theoretical perspective, as one of the most important cornerstone of microcantilever-based static detection technology, the curvature analysis based Stoney's formula has been widely used to describe the quantitative relationship between the surface stress and bending deformation of microcantilever under the essential assumption of uniform curvature deformation[13–14]. Nevertheless, many experiments reveal that the uniform deformation assumption-based Stoney's formula might lose efficiency in several cases, such as relatively large deflection and relatively thick coating on substrate[15–16]. Meanwhile, by coupling the extended finite element/level set method (XFEM), Farsad et al.[12] demonstrated that the surface-stress-driven strain relaxation of a fix/free nanoplate would inevitably induce the non-uniform displacement distribution and its effective bending stiffness. As a matter of fact, Stoney's formula originates from the perspective of pure bending which approximates surface stress as a corresponding concentrated moment at the free-end of microcantilever[17]. However, under certain experimental conditions, this approximation might be unreasonable.

In order to further clarify the surface stress effect on detection signals, some scholars have made a lot of progresses in the sense of surface stress induced non-uniform deformation. By using the nonlocal elasticity theory, Li et al.[18] showed that the bending of a beam subjected to general transverse distributed loads was significantly influenced by the nonlocal scale effect, which would further change the static deformation. As a matter of fact, Eringen[19] has demonstrated that the nonlocal effect was related to the surface stress effect. By using the classical elasticity theory, Sader et al.[20] focused on the aspect ratio effect on the curvature distribution of microcantilever, and showed that the traditional assumption of uniform curvature was quite extreme, and the clamped-end effect on the static deflection of microcantilever should be considered when the aspect ratio was relatively small. Considering the effect of boundary conditions and surface-induced fields, Yi and Duan[21] discussed the contribution of tangential Coulomb force and van der Waals force on the surface stress, and explored the influence of the intrinsic strain and surface stress on the microcantilever deflection. Yue et al.[22] developed a continuum Euler-Bernoulli model for the piezoelectric nanobeam with surface effects, and compared it with the traditional Young-Laplace model. They concluded that the surface model without induced fields would overestimate the surface stress effects. Singh and Yadava[23] investigated the influence of geometric nonlinear high-order terms caused by neutral axis shift on microcantilever response, and revealed that the influence of higher order deformation terms on the system response should be considered in the case of relative large deformation. Based on the classical Donnell's shell theory and von Karman's hypothesis, Ansari et al.[24] discussed the surface stress effect on the static nonlinear buckling and postbuckling behaviors of nanoshells, and illustrated the influence of the surface residual tension and radius-to-thickness ratio. Zhang et al.[17] thoroughly compared the differences of static deflection predicted by three different equivalent surface stress models. However, in the above models, the surface stress is mostly regarded as a concentrated load, but for microcantilever-based biosensors for static detection, those approximately concentrated load models obviously disobey the zero force boundary condition at the free-end of microcantilever.

This paper aims to develop an effective mechanical model for static detection signals of DNA-microcantilever, considering the clamped-end effect which implies the inhomogeneous ef-

fect of the static deformation induced by the clamped-end constraint. First, complying with the zero force boundary condition at free-end, DNA adsorption is taken as an equivalent uniformly distributed tangential load on the upper surface of substrate. Thereout, by using the principle of minimum potential energy, the static governing equation is established to describe the non-uniform deformation of DNA-microcantilever induced by the clamped-end effect. The degradation of the present mechanical model is verified under three different approximate conditions. Second, by reducing the order of the variable coefficient differential governing equation, the analytical solutions of curvature distribution and static bending deflection are obtained, which are verified by numerical method and finite element simulation.

2 Mathematical model

The structure and the relevant coordinate system of a DNA-microcantilever are shown in Fig. 1, where DNA adsorption is taken as an equivalent external uniformly distributed tangential load (τ_{s}, N/m) on the upper surface of substrate as in the previous relevant studies[17]. According to the previous static deformation analysis of DNA-microcantilever[25], the influence of adsorbate stiffness on the deflection of microcantilever can be ignored when the thickness of the adsorption film is relatively thin. According to the microbeam experiments in Ref. [26], the substrate is considered as an asymmetric three-layer laminated beam with the length of l and the width of b. The materials of three layers are taken as SiN_4, Cr, and Au with E_{si} and h_{si} ($i = 1, 2, 3$) representing the elastic modulus and thickness of each layer, respectively. The x-axis is established at the geometric mid-plane of the SiN_4 layer, and the positive direction of the z-axis points to the bottom surface.

2.1 Model for static deformation of DNA-microcantilever

In this subsection, the static governing equation of DNA-microcantilever under eccentric loading of uniformly distributed tangential surface load will be established by using the principle of minimum potential energy, i.e., $\delta\Pi - \delta W = 0$, where Π is the deformation potential energy of microcantilever, and W is the external work done by the surface stress.

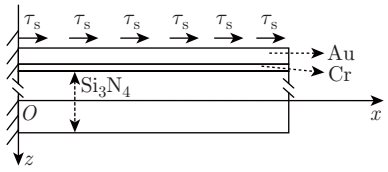

Fig. 1 Schematic diagram of the microcantilever model for static DNA detection, where the equivalent uniformly distributed tangential surface stress τ_{s} is loaded on the upper surface of the substrate

First, the external work of the surface stress is considered. As shown in Fig. 1, the external force at the upper surface of substrate which equals the axial force of the DNA film can be written as $F(x) = \tau_{\mathrm{s}}(l - x)$ based on the undeformed position. This indicates that $F(0) = \tau_{\mathrm{s}} l$, $F(1) = 0$[17]. Obviously, the zero external force at the free-end coincides with the zero force boundary condition at the free-end, which compensates the deficiency of the previous concentrated load models[17,20,27]. In addition, according to the experiments for the DNA film under uniaxial compression shown in Refs. [25] and [28], the adsorption-induced axial stress of the DNA film can be easily obtained as

$$\sigma_{\mathrm{u}} = 3\eta \frac{\partial W_{\mathrm{u}}}{\partial \varepsilon_{\mathrm{u}}}\bigg|_{\varepsilon_{\mathrm{u}}=0},$$

where η is the DNA packing density, and $\eta = 2/(\sqrt{3}d^2)$ is for the hexagonal packing pattern,

where d is the interaxial distance between two parallel DNA cylinders. b_{u} and h_{u} are the width and thickness of the DNA film, respectively. The thickness of the DNA film is $h_{\mathrm{u}} \approx N_{\mathrm{n}} a_{\mathrm{n}}$, where N_{n} is the nucleotide number of DNA, and a_{n} is the nucleotide length directly obtained from STM experiment[29]. ε_{u} is the axial strain of the DNA film, W_{u} is the mesoscopic free energy per unit length of the DNA film, and its specific expression is shown in Appendix A[34–35]. Therefore, the effective surface stress induced by DNA adsorption is predicted as $\tau_{\mathrm{s}} = b_{\mathrm{u}} h_{\mathrm{u}} \sigma_{\mathrm{u}} / l$.

Under the assumption of small deformation, by Zhang's two variable method for deformation field of laminated beam[30], the external force work of the whole microcantilever done by the axial external force $F(x)$ at the position of the upper surface can be approximately written as

$$W = \int_0^l F(x) \mathrm{d}U = \int_0^l \tau_{\mathrm{s}}(l-x)\Big(\frac{\partial u}{\partial x} + \Big(\frac{1}{2}h_{\mathrm{s1}} + h_{\mathrm{s2}} + h_{\mathrm{s3}}\Big)\frac{\partial^2 w}{\partial x^2} - \frac{1}{2}\Big(\frac{\partial w}{\partial x}\Big)^2\Big)\mathrm{d}x, \tag{1}$$

where $\mathrm{d}U$ is the axial displacement of microelement $\mathrm{d}x$ at the position of the upper surface. The derivation processes are shown in Appendix B. u is the x-direction displacement. w is the z-direction displacement.

Second, according to the previous studies[28], the deformation potential energy of the whole microcantilever can be written as

$$\Pi = \int_V \frac{1}{2}\sigma\varepsilon \mathrm{d}V = \int_0^l \Big(\frac{1}{2}D_{\mathrm{s}}^{(0)}\Big(\frac{\partial u}{\partial x}\Big)^2 - D_{\mathrm{s}}^{(1)}\frac{\partial u}{\partial x}\frac{\partial^2 w}{\partial x^2} + \frac{1}{2}D_{\mathrm{s}}^{(2)}\Big(\frac{\partial^2 w}{\partial x^2}\Big)^2\Big)\mathrm{d}x, \tag{2}$$

in which

$$D_{\mathrm{s}}^{(0)} = \sum_{i=1}^{3} b\int_{h_i}^{h_{i+1}} E_{\mathrm{s}i}\mathrm{d}z, \quad D_{\mathrm{s}}^{(1)} = \sum_{i=1}^{3} b\int_{h_i}^{h_{i+1}} E_{\mathrm{s}i} z\mathrm{d}z, \quad D_{\mathrm{s}}^{(2)} = \sum_{i=1}^{3} b\int_{h_i}^{h_{i+1}} E_{\mathrm{s}i} z^2\mathrm{d}z, \tag{3}$$

where σ and ε represent the stress and strain of the substrate, and $\varepsilon = \frac{\partial u}{\partial x} - z\frac{\partial^2 w}{\partial x^2}$[28,30], V is the substrate volume, h_i and h_{i+1} represent the coordinates of the upper and lower surfaces of each layer, $D_{\mathrm{s}}^{(0)}$ is the sum of tension stiffness of each layer, $D_{\mathrm{s}}^{(1)}$ is the sum of tension-bending coupling stiffness of each layer, and $D_{\mathrm{s}}^{(2)}$ is the sum of bending stiffness of each layer. Note that the above deformation energy covers three parts, i.e., tension energy, bending-tension coupling energy, and bending energy.

Combining the stationary condition of energy functional, $\delta\Pi - \delta W = 0$, with Eqs. (1) and (2), we can easily obtain the following equation:

$$\begin{aligned}
&\int_0^l \Big(- \tau_{\mathrm{s}}(l-x)\frac{\partial^2 w}{\partial x^2} + \tau_{\mathrm{s}}\frac{\partial w}{\partial x}\Big)\delta w\mathrm{d}x + D_{\mathrm{s}}^{(0)}\frac{\partial u}{\partial x}\delta u\Big|_0^l - D_{\mathrm{s}}^{(0)}\int_0^l \frac{\partial^2 u}{\partial x^2}\delta u\mathrm{d}x \\
&- D_{\mathrm{s}}^{(1)}\Big(\frac{\partial^2 w}{\partial x^2}\delta u\Big|_0^l + \frac{\partial u}{\partial x}\frac{\partial \delta w}{\partial x}\Big|_0^l - \frac{\partial^2 u}{\partial x^2}\delta w\Big|_0^l - \int_0^l \frac{\partial^3 w}{\partial x^3}\delta u\mathrm{d}x + \int_0^l \frac{\partial^3 u}{\partial x^3}\delta w\mathrm{d}x\Big) \\
&+ D_{\mathrm{s}}^{(2)}\Big(\frac{\partial^2 w}{\partial x^2}\frac{\partial \delta w}{\partial x}\Big|_0^l - \frac{\partial^3 w}{\partial x^3}\delta w\Big|_0^l + \int_0^l \frac{\partial^4 w}{\partial x^4}\delta w\mathrm{d}x\Big) - \tau_{\mathrm{s}}(l-x)\delta u\Big|_0^l \\
&- \int_0^l \tau_{\mathrm{s}}\delta u\mathrm{d}x + \tau_{\mathrm{s}}(l-x)\Big(\frac{1}{2}h_{\mathrm{s1}} + h_{\mathrm{s2}} + h_{\mathrm{s3}}\Big)\frac{\partial \delta w}{\partial x}\Big|_0^l \\
&- \tau_{\mathrm{s}}\Big(\frac{1}{2}h_{\mathrm{s1}} + h_{\mathrm{s2}} + h_{\mathrm{s3}}\Big)\delta w\Big|_0^l + \tau_{\mathrm{s}}(l-x)\frac{\partial w}{\partial x}\delta u\Big|_0^l = 0.
\end{aligned} \tag{4}$$

Next, by using Eq. (4) and the principle of arbitrariness of virtual displacement, the static governing equation of DNA-microcantilever under eccentric loading of uniformly distributed

tangential surface stress is obtained as

$$-D_{\mathrm{s}}^{(1)}\frac{\partial^3 u}{\partial x^3}+D_{\mathrm{s}}^{(2)}\frac{\partial^4 w}{\partial x^4}-\tau_{\mathrm{s}}(l-x)\frac{\partial^2 w}{\partial x^2}+\tau_{\mathrm{s}}\frac{\partial w}{\partial x}=0, \tag{5a}$$

$$-D_{\mathrm{s}}^{(0)}\frac{\partial^2 u}{\partial x^2}+D_{\mathrm{s}}^{(1)}\frac{\partial^3 w}{\partial x^3}-\tau_{\mathrm{s}}=0. \tag{5b}$$

Finding the first derivative of Eq. (5b) with respect to x and substituting the expression of $\frac{\partial^3 u}{\partial x^3}$ into Eq. (5a), the governing equation in terms of w can be written as

$$D^*\frac{\partial^4 w}{\partial x^4}-\tau_{\mathrm{s}}(l-x)\frac{\partial^2 w}{\partial x^2}+\tau_{\mathrm{s}}\frac{\partial w}{\partial x}=0, \tag{6}$$

where D^* represents the effective bending stiffness of the DNA-microcantilever system, and $D^*=D_{\mathrm{s}}^{(2)}-(D_{\mathrm{s}}^{(1)})^2/D_{\mathrm{s}}^{(0)}$, in which $-(D_{\mathrm{s}}^{(1)})^2/D_{\mathrm{s}}^{(0)}$ is induced by the neutral axis shift effect in asymmetric laminated structure. In addition, the third term in Eq. (6) $\tau_{\mathrm{s}}\frac{\partial w}{\partial x}$ is contributed by the clamped-end effect with the same expression in Ref. [17].

Meanwhile, according to Eq. (4), the boundary conditions in terms of axial force, bending moment, and shear force at the free-end are given as follows:

$$\begin{cases} D_{\mathrm{s}}^{(0)}\dfrac{\partial u}{\partial x}\Big|_{x=l}-D_{\mathrm{s}}^{(1)}\dfrac{\partial^2 w}{\partial x^2}\Big|_{x=l}=0, \\ -D_{\mathrm{s}}^{(1)}\dfrac{\partial u}{\partial x}\Big|_{x=l}+D_{\mathrm{s}}^{(2)}\dfrac{\partial^2 w}{\partial x^2}\Big|_{x=l}=0, \\ D_{\mathrm{s}}^{(1)}\dfrac{\partial^2 u}{\partial x^2}\Big|_{x=l}-D_{\mathrm{s}}^{(2)}\dfrac{\partial^3 w}{\partial x^3}\Big|_{x=l}-\tau_{\mathrm{s}}\Big(\dfrac{1}{2}h_{\mathrm{s}1}+h_{\mathrm{s}2}+h_{\mathrm{s}3}\Big)=0. \end{cases} \tag{7}$$

It can be easily seen from Eq. (7) that the uniformly distributed surface stress model exactly satisfies the natural boundary conditions. That is to say, the axial force and bending moment at the free-end should be zero.

By using Eq. (5b), the boundary conditions can be decoupled as

$$u|_{x=0}=0,\quad w|_{x=0}=0,\quad \frac{\partial w}{\partial x}\Big|_{x=0}=0, \tag{8a}$$

$$\begin{cases} \dfrac{\partial u}{\partial x}\Big|_{x=l}=0,\quad \dfrac{\partial^2 w}{\partial x^2}\Big|_{x=l}=0, \\ D^*\dfrac{\partial^3 w}{\partial x^3}\Big|_{x=l}=-\tau_{\mathrm{s}}\Big(\dfrac{1}{2}h_{\mathrm{s}1}+h_{\mathrm{s}2}+h_{\mathrm{s}3}\Big)-\tau_{\mathrm{s}}\dfrac{D_{\mathrm{s}}^{(1)}}{D_{\mathrm{s}}^{(0)}}. \end{cases} \tag{8b}$$

Note that the last term of Eq. (8b), i.e., $(D_{\mathrm{s}}^{(1)}/D_{\mathrm{s}}^{(0)})\tau_{\mathrm{s}}$, is induced by the neutral axis shift effect in asymmetric laminated structure.

Introducing the dimensionless variables and parameters

$$x=\overline{x}l,\quad w=\overline{w}\sqrt{\frac{D^*}{D_{\mathrm{s}}^{(0)}}},\quad t=\overline{t}\sqrt{\frac{ml^4}{D^*}} \tag{9}$$

yields the following dimensionless governing equation:

$$\frac{\partial^4 w}{\partial x^4}-p(1-x)\frac{\partial^2 w}{\partial x^2}+p\frac{\partial w}{\partial x}=0, \tag{10}$$

where $p=\tau_{\mathrm{s}}l^3/D^*$, and the dimensionless boundary conditions can be written as

$$u|_{x=0}=0,\quad w|_{x=0}=0,\quad \frac{\partial w}{\partial x}\Big|_{x=0}=0, \tag{11a}$$

$$\begin{cases}\dfrac{\partial u}{\partial x}\Big|_{x=l}=0,\quad \dfrac{\partial^2 w}{\partial x^2}\Big|_{x=l}=0,\\[2ex] \dfrac{\partial^3 w}{\partial x^3}\Big|_{x=l}=-p\Big(\dfrac{1}{2}h_{\mathrm{s}1}+h_{\mathrm{s}2}+h_{\mathrm{s}3}\Big)\sqrt{\dfrac{D_{\mathrm{s}}^{(0)}}{D^*}}-\dfrac{D_{\mathrm{s}}^{(1)}}{D_{\mathrm{s}}^{(0)}}p\sqrt{\dfrac{D_{\mathrm{s}}^{(0)}}{D^*}}.\end{cases} \tag{11b}$$

Thereout, we have established the governing equation (10) and boundary conditions (11) which exactly satisfy the displacement and force constraints.

2.2 Comparison of surface stress models

In this subsection, some degeneration cases of the present mechanical model under the following three different approximate conditions will be discussed.

(i) When the thicknesses of the Cr and Au layers are relatively thin, the effect of neutral axis shift on the static response of the DNA-microcantilever system can be ignored. In this case, the governing equation (6) and boundary conditions (8) are in consistent with those of Zhang's distributed force-moment model[17].

(ii) When the distributed surface stress on the upper surface of the substrate is approximated as a couple of concentrated force and bending moment at the free-end, the dimensionless axial force $N=p$, which means that the axial force is a constant and the added term in the clamped-end boundary condition will disappear. In this case, the governing equation and boundary conditions are consistent with those of Zhang's concentrated force-moment model[17], and can be written as

$$\begin{cases}\dfrac{\partial^4 w}{\partial x^4}-N\dfrac{\partial^2 w}{\partial x^2}=0,\quad w|_{x=0}=0,\quad \dfrac{\partial w}{\partial x}\Big|_{x=0}=0,\\[2ex] \dfrac{\partial^2 w}{\partial x^2}\Big|_{x=l}=N\Big(\dfrac{1}{2}h_{\mathrm{s}1}+h_{\mathrm{s}2}+h_{\mathrm{s}3}\Big)\sqrt{\dfrac{D_{\mathrm{s}}^{(0)}}{D^*}},\quad \dfrac{\partial^3 w}{\partial x^3}\Big|_{x=l}=N\dfrac{\partial w}{\partial x}.\end{cases} \tag{12}$$

(iii) When the axial force effect induced by DNA adsorption is ignored, the microcantilever deformation is approximately taken as constant curvature bending. In this case, Eq. (12) can be further reduced to the following simplified model related to the classic Stoney's formula[17]:

$$\begin{cases}\dfrac{\partial^4 w}{\partial x^4}=0,\quad w|_{x=0}=0,\quad \dfrac{\partial w}{\partial x}\Big|_{x=0}=0,\\[2ex] \dfrac{\partial^2 w}{\partial x^2}\Big|_{x=l}=N\Big(\dfrac{1}{2}h_{\mathrm{s}1}+h_{\mathrm{s}2}+h_{\mathrm{s}3}\Big)\sqrt{\dfrac{D_{\mathrm{s}}^{(0)}}{D^*}},\quad \dfrac{\partial^3 w}{\partial x^3}\Big|_{x=l}=0.\end{cases} \tag{13}$$

2.3 Analytical prediction for static signals of DNA-microcantilever

As for the variable coefficient differential equation (10), it is usually difficult to obtain the analytical form of its general solution. Referring to the previous analysis of microcantilever large deformation[23], we manage to reduce the order of Eq. (10) by introducing the cross-sectional rotation angle $\theta=\frac{\partial w_{\mathrm{s}}}{\partial x}$. Then, we obtain the governing equation in terms of the rotation angle

$$\frac{\partial^3\theta}{\partial x^3}-p(1-x)\frac{\partial\theta}{\partial x}+p\theta=0 \tag{14}$$

and the relevant boundary conditions

$$\theta|_{x=0} = 0, \tag{15a}$$

$$\frac{\partial\theta}{\partial x}\Big|_{x=l} = 0, \quad \frac{\partial^2\theta}{\partial x^2}\Big|_{x=l} = -p\Big(\frac{1}{2}h_{s1} + h_{s2} + h_{s3}\Big)\sqrt{\frac{D_s^{(0)}}{D^*}} - \frac{D_s^{(1)}}{D_s^{(0)}}p\sqrt{\frac{D_s^{(0)}}{D^*}} = Q. \tag{15b}$$

With the MATHEMATICA software, the general solution to Eq. (14) can be obtained as

$$\begin{aligned}\theta =& 3^{-2/3}(c_1 + \sqrt{3}c_2)\xi_2\Big(\frac{2}{3}, -\frac{1}{9}(x-1)^3\Big)\\ &+ c_3(x-1)^2\xi_1\Big(\frac{4}{3}, -\frac{1}{9}p(x-1)^3\Big)\xi_3\Big(\frac{1}{3}, \Big(\frac{2}{3}, \frac{4}{3}\Big), -\frac{1}{9}p(x-1)^3\Big)\\ &- \frac{1}{2}c_3(x-1)^2\xi_1\Big(\frac{2}{3}, -\frac{1}{9}p(x-1)^3\Big)\xi_3\Big(\frac{2}{3}, \Big(\frac{4}{3}, \frac{5}{3}\Big), -\frac{1}{9}p(x-1)^3\Big),\end{aligned} \tag{16}$$

where ξ_1, ξ_2, and ξ_3 are the confluent hypergeometric function, the regularized confluent hypergeometric function, and the generalized confluent hypergeometric function, receptively. c_1, c_2, and c_3 are determined by the boundary conditions, whose specific expressions are shown in Appendix C.

Eventually, the microcantilever curvature under uniformly distributed tangential surface stress is obtained as

$$\kappa = \frac{\partial^2 w}{\partial x^2} = \frac{\partial\theta}{\partial x}. \tag{17}$$

3 Results and discussion

3.1 Static response of DNA-microcantilever

First, the axial distribution of microcantilever curvature induced by DNA adsorption is studied. Figure 2 shows the accurate analytical predictions from Eq. (17), the approximate numerical solutions from Eq. (10) and solved by the built-in algorithm NDSolve in Mathematica software, and the 3D finite element simulation results obtained by the ANSYS software.

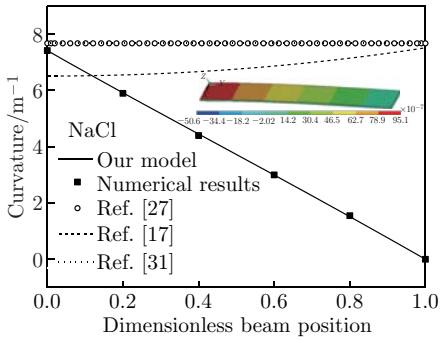

Fig. 2 Comparison of the microcantilever curvature axial distribution induced by the DNA adsorption predicted by different models, where the inset shows the axial distribution of microcantilever strain predicted by the finite element simulation (color online)

In the computation, the DNA parameters are taken as[26]

$$N_n = 25\,\text{nt}, \quad a_n = 0.34, \quad \eta = 0.12\,\text{chain/nm}^2,$$

where $N_{\rm n}$ is the nucleotide number, $a_{\rm n}$ is the nucleotide length, and η is the packing density; the substrate parameters are taken as

$$\begin{cases} l = 200\,\mu\text{m}, \quad b = 10\,\mu\text{m}, \\ h_{\rm s1} = 2\,\mu\text{m}, \quad h_{\rm s2} = 0.005\,\mu\text{m}, \quad h_{\rm s2} = 0.1\,\mu\text{m}, \\ E_{\rm s1} = 180\,\text{GPa}, \quad E_{\rm s2} = 279\,\text{GPa}, \quad E_{\rm s3} = 78\,\text{GPa}, \\ \nu_{\rm s1} = 0.28, \quad \nu_{\rm s2} = 0.12, \quad \nu_{\rm s3} = 0.42, \end{cases}$$

where l, b, and $h_{\rm s1}$ are the geometrical sizes, $E_{\rm s1}$, $E_{\rm s2}$, and $E_{\rm s3}$ are the elastic moduli, and $\nu_{\rm s1}$, $\nu_{\rm s2}$, and $\nu_{\rm s3}$ are Poisson's ratios.

In the finite element simulation, in order to simulate the externally loaded uniformly distributed tangential load, the surface stress induced by the DNA adsorption is taken as the nodal force along the x-direction, applying on the nodes of each mesh element on the upper surface of the substrate. In addition, the element Solid 185 is selected for calculation. In order to ensure the element independence of the simulation results, the grid element size is carefully controlled to 1 nm.

As shown in Fig. 2, the predictions of the DNA adsorption-induced curvature by different models are basically on the same order, and the predictions of our analytical model are in good agreement with the numerical solution of Eq. (10) solved by Mathematica software. It should be mentioned that, neglecting the contribution of the thinner Cr and Au layers, the two-dimensional plate correction model of Tamayo et al. only considers Poisson's effect of the SiN_4 layer[31]. Under the given parameters, the curvature distributions predicted by Tamayo's model[31] and Stoney's model[27] are basically coincident with the uniformly distributed rule along the axial direction. Whereas the curvature, by Zhang's concentrated force-moment model[17], increases monotonously along the axial direction, with its free-end curvature basically consistent with those by Tamayo model[31] and Stoney's model[27]. However, different from the predictions by the above approximate models under concentrated load assumption, the curvature distribution predicted by the present uniformly distributed surface stress model is more closer to the physical reality. That is to say, the microcantilever curvature has the largest value at the clamped-end, decreases almost with a linear trend, and approximates zero at the free-end. The insert of Fig. 2 also shows that the axial strain has the largest value at the clamped-end, and is close to zero at the free-end. The demonstration of these inhomogeneous deformations further confirms the necessity of our model.

Figures 3 and 4 shows the comparison of microcantilever deflections predicted by different models with finite element simulation. Except for the beam length, the calculation conditions are taken as the same as those in Fig. 2. The relative error of different model predictions is defined as

$$((w_{\rm s} - w_{\rm F})/w_{\rm F}) \times 100\%,$$

where $w_{\rm F}$ is the finite element simulation result. As discussed in Fig. 2, the curvature decreases linearly along the axis. Therefore, the approximate analytical solution of microcantilever deflection can be given as

$$w = \rho_0 x^2/2 - \rho_0 x^3/(6l),$$

where ρ_0, obtained by Eq. (17), is the microcantilever curvature at the clamped-end. Figure 3(a) shows the variation of microcantilever deflection with the aspect ratio predicted by different models using the uniaxial modulus $E_{{\rm s}i}$. In this case, the microcantilever width is taken as $b = 10$ μm. The inset of Fig. 3(a) shows the element independence of the finite element simulation. As shown in Fig. 3(a), the analytical predictions by our model agree well with the finite element simulation results. It can be easily seen from Fig. 3(b) that except for our distributed

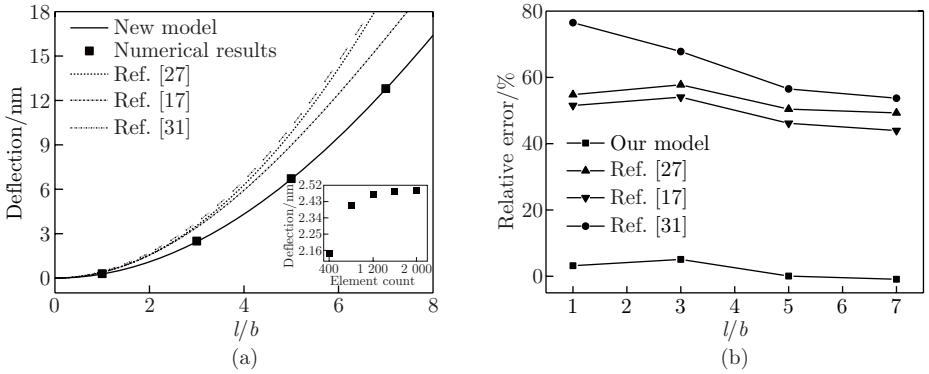

Fig. 3 Comparison of microcantilever deflection prediction varying with the aspect ratio l/b by different models with finite element simulation: (a) deflection prediction by different models using the uniaxial modulus E_{si}; (b) relative error in the case of (a). The results of our model in this figure are consistent with those in Fig. 2

surface stress model, the predictions by other models have larger errors. In fact, based on the assumption of equal strain in the x- and y-directions, the biaxial modulus $E_{si}/(1-\nu_i)$ is usually used to correct the error of the analytical prediction in the traditional deformation analysis of microcantilever[32–33].

Figure 4(a) shows the deflection predictions by different models using the biaxial modulus $E_{si}/(1-\nu_i)$, whereas the uniaxial modulus E_{si} is still used in our distributed surface stress model. Note that in Fig. 4(a), the prediction by each concentrated load model with biaxial modulus correction is much closer to the finite element results, which shows the rationality of biaxial modulus correction in the previous expedient analysis. However, it can be seen from the relative error analysis in Fig. 4(b), although the biaxial modulus correction may improve the prediction accuracy of each approximate concentrated load model to a certain extent, the relative error of each prediction result is still more than 5% under some parameter conditions. In addition, when the aspect ratio l/b is smaller than 5, the relative prediction error of our distributed surface stress models is still larger than 5%. Under this condition, Zhang's distributed stress-moment model is more accurate[17]. Furthermore, when the aspect ratio l/b is larger than 5, the relative prediction error of our distributed surface stress model is less than 1%. In this range, the present distributed surface stress model is more accurate than the approximate concentrated load models, which reflects the superiority of our model. As the discussion of Fig. 4, based on the assumption of equal strain in x and y directions, the biaxial modulus correction efficiently improves the prediction accuracy of each approximate concentrated load model to a certain extent. In the following section, we will further discuss the rationality of the equivalent strain assumption based on finite element simulation.

Figures 5(a) and 5(b) show the strain distribution of the microcantilever in the x- and y-directions, respectively. By comparison, we can easily observe that the strains in the x- and y-directions differ by about an order of magnitude at the clamped-end (left side). Due to the clamped-end effect, even at the free-end (right side), the strains in the two directions have a difference of four time orders of magnitude. These results indicate that the equal strain assumption is invalid in the local strain field. However, from the point of simplicity, the biaxial modulus based on equal strain assumption reasonably modifies the deflection prediction error from the perspective of the overall average of the strain field.

3.2 Application range of existing concentrated load models

In this section, under the circumstance of relatively larger aspect ratio ($l/b > 5$), the application scope of the previous concentrated load models based on the biaxial modulus

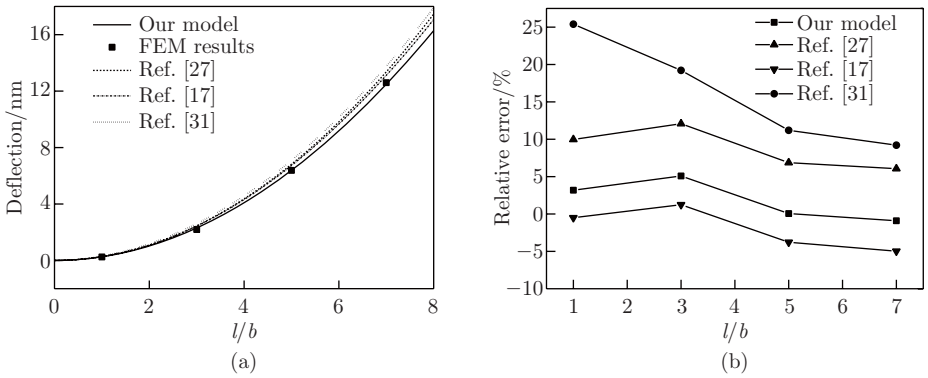

Fig. 4 Comparison of microcantilever deflection prediction varying with the aspect ratio l/b by different models with finite element simulation: (a) deflection prediction by different models using the biaxial modulus $E_{si}/(1-\nu_i)$, whereas the uniaxial modulus E_{si} is still used in our distributed surface stress model; (b) relative error in the case of (a). The results of our model in this figure are consistent with those in Fig. 2

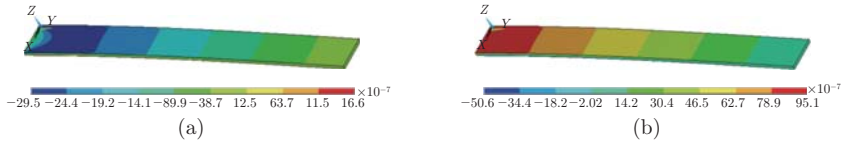

Fig. 5 Finite element simulation of microcantilever deformation: (a) x-direction strain field; (b) y-direction strain field (color online)

correction will be checked by the benchmark of our analytical deflection predictions, i.e., $w = \rho_0 x^2/2 - \rho_0 x^3/(6l)$.

Figure 6 shows the projection of the $\pm 10\%$ relative error of deflection prediction by each concentrated load model in the parameter plane, which is spanned by the aspect ratio l/b and the DNA packing density η. The relative error is defined as $((w_{\rm s} - w_{\rm D})/w_{\rm D}) \times 100\%$, where $w_{\rm D}$ is the deflection predicted by our distributed surface stress model. Except for the beam length l and DNA packing density η, other parameters are taken the same as those in Fig. 3.

As shown in Fig. 6, within the range of selected parameter space, the deflection predictions by Stoney's concentrated moment model[27] and Tamayo's two-dimensional plate model[31] are always overestimated. However, the deflection prediction by Zhang's concentrated stress-moment model[17] is always underestimated. In addition, for Stoney's concentrated moment model[27] and Zhang's concentrated stress-moment model[17], the lower left part of the curve represents the parameter interval with the absolute value of relative prediction error less than 10%, which means that the prediction are reliable when the DNA packing density and aspect ratio are relatively small. For Tamayo's two-dimensional plate model[31], the upper left part of the curve represents the parameter interval with the relative prediction error less than 10%, which means that the prediction are reliable only when the DNA packing density $\eta < 0.131$ chain/nm^2.

3.3 Influence of neutral axis shift effect on the deflection of microcantilever

In this section, we will discuss the influence of the neutral axis shift effect induced by the characteristics of asymmetric laminated structure on the static deflection of microcantilever. From the governing equations (6) and boundary conditions (8), it is not difficult to identify that the contribution of the neutral axis shift effect in microcantilever static responses can be divided into two parts, i.e., the change in equivalent bending stiffness and change in boundary

conditions.

Figure 7 shows the projection of the 10% relative error in the parameter plane, the relative error is defined as $((w_{\mathrm{N}} - w_{\mathrm{D}})/w_{\mathrm{D}}) \times 100\%$, where w_{N} is the deflection predicted by our distributed surface stress model when the neutral axis drift effect is neglected. The parameter plane is spanned by the elastic modulus E_{s1} of the SiN_4 layer and the thickness thickness ratio $h_{\mathrm{s1}}/(h_{\mathrm{s2}} + h_{\mathrm{s3}})$ of the Cr and Au layers. The microcantilever length is taken as $l = 10\,\mu\mathrm{m}$, the width is taken as $b = 1\,\mu\mathrm{m}$, except for the elastic modulus E_{s1} and thickness h_{s1} of substrate layer, other parameters are taken the same as those in Fig. 2.

As shown in Fig. 7, the deflection prediction is always overestimated when the effect of neutral axis drift is ignored. In addition, the shadow area in Fig. 7 represents the parameter space with the relative error greater than 10%, which means that the influence of the neutral axis shift effect on the deflection prediction of the laminated beam should be considered when the substrate elastic modulus is relatively smaller or the substrate thickness is relatively thinner.

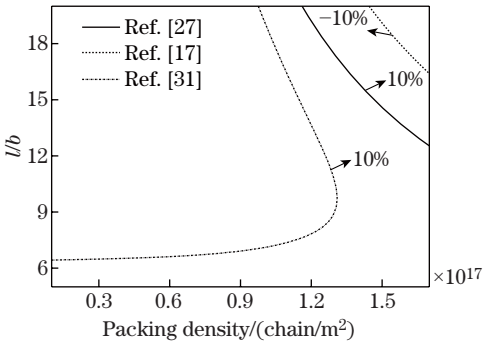

Fig. 6 Application scope of existing concentrated load models based on the biaxial modulus correction by taking our analytical prediction as a benchmark. The results of our model in this figure are consistent with those in Fig. 2

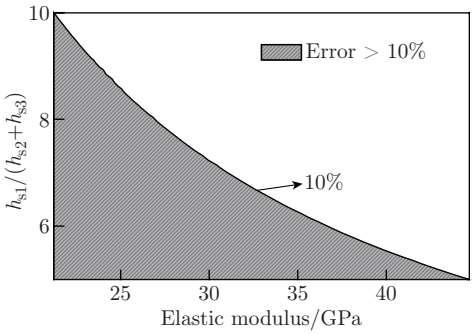

Fig. 7 Projection of 10% relative error of deflection prediction by our distributed surface stress model when the neutral axis shift effect is neglected in the parameter plane

4 Conclusions

In this paper, an eccentric and uniform loading model of surface stress is established to characterize the influence of inhomogeneous deformation field induced by DNA adsorption and clamped-end constraint on the static deflection of microcantilever biosensor. Strictly complying with displacement and force boundary conditions at the free-end, an exact solution for axial distribution of microcantilever curvature is presented to clarify the clamped-end effect and the neutral axis shift effect. The related predictions agree well with the numerical solutions of MATHEMATICA and 3D finite element simulations of ANAYS. The comparative analyses reveal that the clamped-end effect makes microcantilever curvature no longer be a constant, whereas it decreases linearly along the axis with the largest value at the clamped-end, and is close to zero at the free-end. In addition, we give out the application range of the existing concentrated load models based on the prevail biaxial modulus correction. The related results provide an important reference for biodetection signal recognition and careful parameter control of microcantilever biosensors.

References

[1] SADER, J. E., HANAY, M. S., NEUMANN, A., and ROUKES, M. L. Mass spectrometry using nanomechanical systems: beyond the point-mass approximation. *Nano Letters*, **18**, 1608–1614 (2018)

[2] ROMOS, D., MALVAR, O., DAVIS, Z. J., TAMAYO, J., and CALLEJA, M. Nanomechanical plasmon spectroscopy of single gold nanoparticles. *Nano Letters*, **18**, 7165–7170 (2018)

[3] VENSTRA, W. J., CAPENER, M. J., and ELLIOTT, S. R. Nanomechanical gas sensing with nonlinear resonant cantilevers. *Nanotechnology*, **25**, 425501 (2014)

[4] STASSI, S., MARINI, M., ALLIONE, M., LOPATIN, S., MARSON, D., LAURINI, E., PRICL, S., PIRRI, C. F., RICCIARD, C., and FABRIZIO, E. D. Nanomechanical DNA resonators for sensing and structural analysis of DNA-ligand complexes. *Nature Communications*, **10**, 1690 (2019)

[5] RU, C. Q. Simple geometrical explanation of Gurtin-Murdoch model of surface elasticity with clarification of its related versions. *Science China* (*Physics*, *Mechanics* & *Astronomy*), **53**, 536–544 (2010)

[6] RAHMANI, O., ASEMANI, S. S., and HOSSEINI, S. A. Study the surface effect on the buckling of nanowires embedded in Winkler-Pasternak elastic medium based on a nonlocal theory. *Journal of Nanostructures*, **6**, 87–92 (2016)

[7] YIN, Y. and CHEN, S. H. Surface effect on resonant properties of nanowires predicted by an elastic theory for nanomaterials. *Journal of Applied Physics*, **118**, 44303 (2015)

[8] SHENOY, V. B. Atomistic calculations of elastic properties of metallic FCC crystal surfaces. *Physical Review B*, **71**, 094104 (2005)

[9] MI, C., JUN, S., KOURIS, D. A., and KIM, S. Y. Atomistic calculations of interface elastic properties in noncoherent metallic bilayers. *Physical Review B*, **77**, 075425 (2008)

[10] NGUYEN, N. T., KIM, N. I., and LEE, J. Mixed finite element analysis of nonlocal Euler-Bernoulli nanobeams. *Finite Elements in Analysis & Design*, **106**, 65–72 (2015)

[11] NOROUZZADEH, A. and ANSARI, R. Finite element analysis of nano-scale Timoshenko beams using the integral model of nonlocal elasticity. *Physica E*: *Low-Dimensional Systems and Nanostructures*, **88**, 194–200 (2017)

[12] FARSAD, M., VERNEREY, F. J., and PARK, H. S. An extended finite element/level set method to study surface effects on the mechanical behavior and properties of nanomaterials. *International Journal for Numerical Methods in Engineering*, **84**, 1466–1489 (2010)

[13] IBACH, H. Adsorbate induced surface stress. *Journal of Vacuum Science & Technology A-Vacuum Surfaces & Films*, **12**, 2240–2245 (1994)

[14] HAISS, W. Surface stress of clean and adsorbate-covered solids. *Reports on Progress in Physics*, **64**, 591–648 (2001)

[15] KLEIN, C. A. and MILLER, R. P. Strains and stresses in multilayered elastic structures: the case of chemically vapor-deposited ZnS/ZnSe laminates. *Journal of Applied Physics*, **87**, 2265–2272 (2000)

[16] FREUND, L. B., FLORO, J. A., and CHASON, E. Extensions of the Stoney formula for substrate curvature to configurations with thin substrates or large deformations. *Applied Physics Letters*, **74**, 1987–1989 (1999)

[17] ZHANG, Y., REN, Q., and ZHAO, Y. P. Modelling analysis of surface stress on a rectangular cantilever beam. *Journal of Physics D*: *Applied Physics*, **37**, 2140–2145 (2004)

[18] LI, C., YAO, L. Q., CHEN, W. Q., and LI, S. Comments on nonlocal effects in nano-cantilever beams. *International Journal of Engineering Science*, **87**, 47–57 (2015)

[19] ERINGEN, A. C. On differential equations of nonlocal elasticity and solutions of screw dislocation and surface waves. *Journal of Applied Physics*, **54**, 4703–4710 (1983)

[20] SADER, E. J. Surface stress induced deflections of cantilever plates with applications to the atomic force microscope: rectangular plates. *Journal of Applied Physics*, **89**, 2911–2921 (2001)

[21] YI, X. and DUAN, H. L. Surface stress induced by interactions of adsorbates and its effect on deformation and frequency of microcantilever sensors. *Journal of the Mechanics and Physics of Solids*, **57**, 1254–1266 (2009)

[22] YUE, Y. M., XU, K. Y., ZHANG, X. D., and WANG, W. J. Effect of surface stress and surface-induced stress on behavior of piezoelectric nanobeam. *Applied Mathematics and Mechanics* (*English Edition*), **39**(7), 953–966 (2018) https://doi.org/10.1007/s10483-018-2346-8

[23] SINGH, P. and YADAVA, R. D. S. Effect of surface stress on resonance frequency of microcantilever sensors. *IEEE Sensors Journal*, **18**, 7529–7536 (2018)

[24] ANSARI, R., POURASHRAF, T., GHOLAMI, R., and ROUHI, H. Analytical solution approach for nonlinear buckling and postbuckling analysis of cylindrical nanoshells based on surface elasticity theory. *Applied Mathematics and Mechanics* (*English Edition*), **37**(7), 903–918 (2016) https://doi.org/10.1007/s10483-016-2100-9

[25] ZHOU, M. H., MENG, W. L., ZHANG, C. Y., LI, X. B., WU, J. Z., and ZHANG, N. H. The pH-dependent elastic properties of a nanoscale DNA film and the resultant bending signals for microcantilever biosensors. *Soft Matter*, **14**, 3028 (2018)

[26] FU, J. Y., CHEN, D. P., YE, T. C., JIAO, B. B., and OU, Y. Modeling and optimal design of multilayer thermal cantilever microactuators. *Science in China*, **52**, 1167–1170 (2009)

[27] STONEY, G. G. The tension of metallic films deposited by electrolysis. *Proceedings of the Royal Society of London*, **82**, 172–175 (1909)

[28] WU, J. Z., ZHANG, Y., and ZHANG, N. H. Anomalous elastic properties of attraction-dominated DNA self-assembled 2D films and the resultant dynamic biodetection signals of microbeam sensors. *Nanomaterials*, **9**, 543 (2019)

[29] REKESH, D., LYUBCHENKO, Y., SHLYAKHTENKO, L. S., and LINDSAY, S. M. Scanning tunneling microscopy of mercapto-hexyl-oligonucleotides attached to gold. *Biophysical Journal*, **71**, 1079–1086 (1996)

[30] ZHANG, N. H. and XING, J. J. An alternative model for elastic bending deformation of multilayered beams. *Journal of Applied Physics*, **100**, 53 (2006)

[31] TAMAYO, J., RUZ, J. J., PINI, V., KOSAKA, P., and CALLEJA, M. Quantification of the surface stress in microcantilever biosensors: revisiting Stoney's equation. *Nanotechnology*, **23**, 475702 (2012)

[32] HSUEH, C. H. Modeling of elastic deformation of multilayers due to residual stresses and external bending. *Journal of Applied Physics*, **91**, 9652–9656 (2002)

[33] RUZ, J. J., PINI, V., MALVAR, O., KOSAKA, P. M., CALLEJA, M., and TAMAYO, J. Effect of surface stress induced curvature on the eigenfrequencies of microcantilever plates. *AIP Advances*, **8**, 105213 (2018)

[34] STREY, H. H., PARSEGIAN, V. A., and PODGORNIK, R. Equation of state for DNA liquid crystals: fluctuation enhanced electrostatic double layer repulsion. *Physical Review Letters*, **78**, 895–898 (1997)

[35] AMBIA-GARRIDO, J., VAINRUB, A., and PETTITT, B. M. A model for structure and thermodynamics of ssDNA and dsDNA near a surface: a coarse grained approach. *Computer Physics Communications*, **181**, 2001–2007 (2010)

Appendix A

Based on a liquid crystal model and osmotic pressure experiments[34], the free energy per unit length between two parallel DNA cylinders is given as

$$W_{\mathrm{u}} = W_{\mathrm{e}} + W_{\mathrm{h}} + W_{\mathrm{c}}, \tag{A1}$$

in which W_{e}, W_{h}, and W_{c} are, respectively, the electrostatic energy, the hydration energy, and the configurational entropy, and

$$W_{\mathrm{e}}(z,d)=a_0\exp(-d/\lambda_{\mathrm{D}})/\sqrt{d/\lambda_{\mathrm{D}}},$$

$$W_{\mathrm{h}}=b_0\exp(-d/\lambda_{\mathrm{H}})/\sqrt{d/\lambda_{\mathrm{H}}},$$

$$W_{\mathrm{c}}=c_0k_{\mathrm{B}}Tk_{\mathrm{c}}^{-1/4}\sqrt[4]{\frac{\partial^2(W_{\mathrm{e}}+W_{\mathrm{h}})}{\partial d^2}-\frac{1}{d}\frac{\partial(W_{\mathrm{e}}+W_{\mathrm{h}})}{\partial d}}, \tag{A2}$$

where d is the interaxial distance between two parallel DNA cylinders, λ_{D} is the Debye screening length, λ_{H} is the correlation length of water, and a_0, b_0, and c_0 are the fitting parameters for DNA interactions[34]. k_{B} is the Boltzmann constant, T is the temperature, $k_{\mathrm{c}}=k_{\mathrm{B}}Tl_{\mathrm{p}}^{\mathrm{ds}}$ is the bending stiffness of a single-molecule dsDNA chain, $l_{\mathrm{p}}^{\mathrm{ds}}$ $(=(50+0.032\,4/I)\,\mathrm{nm})$ is the persistence length of dsDNA, and I is the buffer salt concentration[35].

Appendix B

As shown in Fig. B1, by applying the traditional practice of elastic mechanics and Zhang's two variable method[30], the length of the deformed microelement can be written as

$$\begin{aligned}\mathrm{d}x'&=(\mathrm{d}s^2-(\theta\mathrm{d}x)^2)^{1/2}\\&=\Big(((1+\varepsilon)\mathrm{d}x)^2-\Big(\Big(\frac{\partial w}{\partial x}\Big)\mathrm{d}x\Big)^2\Big)^{1/2}\\&\approx\Big(1+2\varepsilon-\Big(\frac{\partial w}{\partial x}\Big)^2\Big)^{1/2}\mathrm{d}x\\&\approx\Big(1+\frac{1}{2}\Big(2\varepsilon-\Big(\frac{\partial w}{\partial x}\Big)^2\Big)\Big)\mathrm{d}x\\&=\Big(1+\varepsilon-\frac{1}{2}\Big(\frac{\partial w}{\partial x}\Big)^2\Big)\mathrm{d}x,\end{aligned} \tag{B1}$$

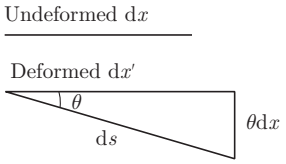

Fig. B1 Deformation state of the microelement $\mathrm{d}x$, where θ is the rotation angle, $\mathrm{d}s$ is the arc length of the deformed microelement, and $\theta\mathrm{d}x$ represents the displacement in the vertical direction

where ε is the axial strain of laminated beam, and

$$\varepsilon=\frac{\partial u}{\partial x}-z\frac{\partial^2 w}{\partial x^2}.$$

Then, from Eq. (B1), we can easily obtain the axial displacement of the microelement $\mathrm{d}x$ at the position of the substrate upper surface as

$$\mathrm{d}U=\mathrm{d}x'-\mathrm{d}x=\Big(\frac{\partial u}{\partial x}+\Big(\frac{1}{2}h_{\mathrm{s1}}+h_{\mathrm{s2}}+h_{\mathrm{s3}}\Big)\frac{\partial^2 w}{\partial x^2}-\frac{1}{2}\Big(\frac{\partial w}{\partial x}\Big)^2\Big)\mathrm{d}x. \tag{B2}$$

Thereout, the external work done by the surface stress is obtained as

$$W=\int_0^l F(x)\mathrm{d}U=\int_0^l\tau_{\mathrm{s}}(l-x)\Big(\frac{\partial u}{\partial x}+\Big(\frac{1}{2}h_{\mathrm{s1}}+h_{\mathrm{s2}}+h_{\mathrm{s3}}\Big)\frac{\partial^2 w}{\partial x^2}-\frac{1}{2}\Big(\frac{\partial w}{\partial x}\Big)^2\Big)\mathrm{d}x, \tag{B3}$$

which can be further separated into

$$W=\int_0^l M_1(x)\frac{\partial^2 w}{\partial x^2}\mathrm{d}x-\frac{1}{2}\int_0^l F_1(x)\Big(\frac{\partial w}{\partial x}\Big)^2\mathrm{d}x+\int_0^l F_1(x)\frac{\partial u}{\partial x}\mathrm{d}x, \tag{B4}$$

where $M_1(x)$ and $F_1(x)$ represent, respectively, the external moment and the external force, and

$$\begin{cases} M_1(x)=\tau_{\mathrm{s}}(l-x)\Big(\dfrac{1}{2}h_{\mathrm{s}1}+h_{\mathrm{s}2}+h_{\mathrm{s}3}\Big), \\ F_1(x)=F(x)=\tau_{\mathrm{s}}(l-x), \end{cases}$$

if one simplifies the surface stress as to the substrate mid-plane[17]. The last term of Eq. (B4) represents the contribution of the neutral axis shift effect to the external work of the eccentrically loaded laminated beam. Note that if the x-axis is relocated at the neutral axis of the substrate, the last term of Eq. (B4) turns to be zero with the axial strain at the neutral axis, i.e., $\varepsilon_0=\frac{\partial u}{\partial x}=0$, and the present form of the external work in Eq. (B4) degenerates into the previous form of Zhang's model[17].

Appendix C

The mathematical forms of various confluence hypergeometric functions in Eq. (16) are as follows.

(i) Confluent hypergeometric function $\xi_1(a,f(x))$

$$\begin{aligned}\xi_1(a,f(x))=&1+\frac{f(x)}{a}+\frac{f^2(x)}{2a(1+a)}+\frac{f^3(x)}{6a(1+a)(2+a)}\\&+\frac{f^4(x)}{24a(1+a)(2+a)(3+a)}+o(f(x))^5.\end{aligned} \tag{C1}$$

(ii) Regularized confluent hypergeometric function $\xi_2(a,f(x))$

$$\begin{aligned}\xi_2(a,f(x))=&\frac{1}{\zeta(a)}+\frac{f(x)}{\zeta(1+a)}+\frac{f^2(x)}{2\zeta(2+a)}\\&+\frac{f^3(x)}{6\zeta(3+a)}+\frac{f^4(x)}{24\zeta(3+a)}+o(f(x))^5,\end{aligned} \tag{C2}$$

where

$$\zeta(a)=\int_0^{+\infty}t^{a-1}\mathrm{e}^{-t}\mathrm{d}t.$$

(iii) Generalized confluent hypergeometric function $\xi_2(a,(b_1,b_2),f(x))$

$$\begin{aligned}\xi_3(a,(b_1,b_2),f(x))=&1+\frac{af(x)}{b_1b_2}+\frac{a(1+a)f(x)}{2b_1b_2(1+b_1)(1+b_2)}\\&+\frac{a(1+a)(2+a)f^3(x)}{6b_1b_2(1+b_1)(2+b_1)(1+b_2)(2+b_2)}\\&+\frac{a(1+a)(2+a)(3+a)f^4(x)}{24b_1b_2(1+b_1)(2+b_1)(1+b_2)(2+b_2)(3+b_2)}+o(f(x))^5.\end{aligned} \tag{C3}$$

The mathematical forms of the undetermined coefficients in Eq. (16) are as follows:

$$\begin{aligned}c_1 =& 3^{19/3}Q\zeta\Big(-\frac{1}{3}\Big)\zeta\Big(\frac{1}{3}\Big)\zeta\Big(\frac{2}{3}\Big)\zeta\Big(\frac{4}{3}\Big)\Big((x-1)^2\xi_1\Big(\frac{4}{3},-\frac{1}{9}p(x-1)^3\Big)\\&\xi_3\Big(\frac{1}{3},\Big(\frac{2}{3},\frac{4}{3}\Big)-\frac{1}{9}p(x-1)^3\Big)-\frac{1}{2}(x-1)^2\xi_1\Big(\frac{2}{3},-\frac{1}{9}p(x-1)^3\Big)\\&\xi_3\Big(\frac{2}{3},\Big(\frac{4}{3},\frac{5}{3}\Big)-\frac{1}{9}p(x-1)^3\Big)\Big)\Big/\Big(4\pi\Big(\zeta\Big(-\frac{1}{3}\Big)\zeta\Big(\frac{1}{3}\Big)+3\zeta\Big(\frac{1}{3}\Big)\zeta\Big(\frac{2}{3}\Big)\\&-3\zeta\Big(-\frac{1}{3}\Big)\zeta\Big(\frac{4}{3}\Big)\Big)\xi_2\Big(\frac{2}{3},-\frac{1}{9}p(x-1)^3\Big)\Big),\end{aligned}\tag{C4}$$

$$\begin{aligned}c_2 =& 3^{5/3}Q\zeta\Big(-\frac{1}{3}\Big)\zeta\Big(\frac{1}{3}\Big)\zeta\Big(\frac{2}{3}\Big)\zeta\Big(\frac{4}{3}\Big)\Big((x-1)^2\xi_1\Big(\frac{4}{3},-\frac{1}{9}p(x-1)^3\Big)\\&\xi_3\Big(\frac{1}{3},\Big(\frac{2}{3},\frac{4}{3}\Big),-\frac{1}{9}p(x-1)^3\Big)-\frac{1}{2}(x-1)^2\xi_1\Big(\frac{2}{3},-\frac{1}{9}p(x-1)^3\Big)\\&\xi_3\Big(\frac{2}{3},\Big(\frac{4}{3},\frac{5}{3}\Big)-\frac{1}{9}p(x-1)^3\Big)\Big)\Big/\Big(4\pi\Big(\zeta\Big(-\frac{1}{3}\Big)\zeta\Big(\frac{1}{3}\Big)+3\zeta\Big(\frac{1}{3}\Big)\zeta\Big(\frac{2}{3}\Big)\\&-3\zeta\Big(-\frac{1}{3}\Big)\zeta\Big(\frac{4}{3}\Big)\Big)\xi_2\Big(\frac{2}{3},-\frac{1}{9}p(x-1)^3\Big)\Big),\end{aligned}\tag{C5}$$

$$\begin{aligned}c_3 =& -3\sqrt{3}Q\zeta\Big(-\frac{1}{3}\Big)\zeta\Big(\frac{1}{3}\Big)\zeta\Big(\frac{2}{3}\Big)\zeta\Big(\frac{4}{3}\Big)\Big/\Big(2\pi\Big(\zeta\Big(-\frac{1}{3}\Big)\zeta\Big(\frac{1}{3}\Big)\\&+3\zeta\Big(\frac{1}{3}\Big)\zeta\Big(\frac{2}{3}\Big)-3\zeta\Big(-\frac{1}{3}\Big)\zeta\Big(\frac{4}{3}\Big)\Big)\Big).\end{aligned}\tag{C6}$$